CFD-Based Frequency Domain Method for Dynamic Control Derivative Estimation with Application to Transonic Truss-Braced Wing

Nhan Nguyen*
NASA Ames Research Center, Moffett Field, CA 94035
Juntao Xiong†
KBR Wyle, Inc., Moffett Field, CA 94035

This paper presents a dynamic control derivative estimation technique obtained from high-fidelity CFD simulations of the Mach 0.8 Transonic Truss-Braced Wing (TTBW). A series of unsteady RANS CFD simulations in FUN3D is performed to simulate the elevator control surface oscillations at various reduced frequencies. The time-domain data are transformed into the frequency-domain data by a Fourier series analysis. Transfer functions of the dynamic control derivatives are then estimated by a frequency-domain regression. The nonlinear effect of control surface deflection amplitude is investigated.

I. Introduction

Vehicle stability and control is an area of study that deals with the design and analysis aspects of aircraft stability and control. Vehicle stability requires that an aircraft design be statically and dynamically stable and controllable in all three axes of the motion in roll, pitch, and yaw. Vehicle control is accomplished by aerodynamic control surfaces or other control effectors.

A stability and control analysis is usually required to determine a set of stability and control derivatives with respect to the aircraft state and control variables. The stability and control derivatives include both steady state derivatives such as C_{m_α},the pitching moment stability derivative with respect to the angle of attack, and $C_{m_{\delta_e}}$, the pitching moment control derivative with respect to the elevator deflection . Dynamic derivatives are the sensitivities evaluated by the partial derivatives with respect to the dynamic state variables of the aircraft such as the pitch rate q and control surface acceleration $\ddot{\delta}_e$. The dynamic stability derivatives with respect to the angular rates p, q, and r generally can be computed by some analytical techniques. On the other hand, dynamic derivatives with respect to the time derivatives of the aircraft state and control variables are more difficult to established. These derivatives account for the time delay in the aerodynamic response of the aircraft which can be important. The steady state and dynamic stability derivatives can be estimated experimentally by stability-and-control wind tunnel experiments or analytically by unsteady flow simulations.

The numerical estimation of dynamic stability and control derivatives is a current research topic. Recent work in this area can be found in many references.[2,3,7] Many of these technique do not adequately capture the various terms of the dynamic stability derivatives. More importantly, the effects of the frequency response on the dynamic stability derivatives is not well addressed especially for aircraft operating in transonic flight regime. Murman uses reduced-frequency approach to address the frequency response, but the approach lacks sufficient details to enable a systematic approach to determining the dynamic stability derivatives.[3] A frequency-domain dynamic stability estimation has recently been developed[4] and applied to the Mach 0.8 Transonic Truss-Braced Wing (TTBW) aircraft,[5] shown in Figure 1. Using unsteady RANS CFD simulation results, the time histories of the aerodynamic coefficients are transformed into the frequency domain by a Fourier series analysis as a function of the reduced frequency. A frequency-domain

*Senior Research Scientist and Technical Group Lead of Advanced Control and Engineering Systems Group, Intelligent Systems Division, nhan.t.nguyen@nasa.gov
†Aerospace Engineer, Intelligent System Division, juntao.xiong@nasa.gov

transfer function is designed to capture both the steady state and dynamic derivatives. The transfer function is formulated based on the Theodorsen's theory.[6] A frequency-domain regression analysis is then performed to estimate the transfer function. The proposed method can estimate those dynamic stability derivatives that are usually not captured in many analyses but do exist in the Theordorsen's theory such as $C_{m_{\dot{q}}}$ due to the apparent mass effect.

Figure 1. Boeing Mach 0.8 Transonic Truss-Braced Wing Aircraft Concept

This study continues the investigation of the stability and control estimation using high-fidelity CFD. In this study, we develop a frequency-domain estimation of the control derivatives for the TTBW. FUN3D unsteady RANS simulations of control surface oscillations of the elevator are conducted for various reduced frequencies from 0.02 to 0.2. The effect of control surface amplitude is studied for various amplitudes of control surface oscillations. In particular, at high deflection amplitudes, significant nonlinearity in the aerodynamic response to the control surface deflections is observed. Techniques are developed to estimate the nonlinear dynamic control derivatives for large control surface deflection amplitudes.

II. Control Derivative Estimation Method

The lift and pitching moment contributions by a 2D section of a control surface is established by Theodorsen's theory.[6] These contributions are given by

$$\Delta c_l = \frac{c_{l_\alpha}}{\pi} C(k) \left(T_{10}\delta + \frac{T_{11}}{2}\frac{c\dot{\delta}}{2V_\infty} \right) - T_4 \frac{c\dot{\delta}}{2V_\infty} - T_1 \frac{c^2\ddot{\delta}}{4V_\infty^2} \tag{1}$$

$$\begin{aligned} \Delta c_m = &\frac{c_{l_\alpha}}{\pi} eC(k) \left(T_{10}\delta + \frac{T_{11}}{2}\frac{c\dot{\delta}}{2V_\infty} \right) - \frac{1}{2}\left(T_4 + T_{10}\right)\delta - \frac{1}{2}\left[\left(T_1 - T_8\right) - e_h T_4 + \frac{1}{2} T_{11} \right] \frac{c\dot{\delta}}{2V_\infty} \\ &+ \frac{1}{2}\left(T_7 + e_h T_1\right) \frac{c^2\ddot{\delta}}{4V_\infty^2} \end{aligned} \tag{2}$$

where c the airfoil chord, $e = x_e - x_{ac}$ is the offset between the center of rotation and the aerodynamic center at the quarter-chord location, $e_h = x_h - x_e$ is the offset between the center of rotation and the hinge, and T_i are defined by Theodorsen. For aircraft, the center of rotation is the center of gravity which is far ahead of the horizontal tail. Then, the second term which is due to the pitching moment about the aerodynamic center of the horizontal tail section is much smaller than the other terms and can be neglected.

Let $\bar{s} = ik$ be a nondimensional Laplace variable and $\tau = \frac{2V_\infty}{c}t$ be a nondimensional time variable. We propose a general expression for the lift and pitching moment coefficients of the form

$$C_L = C_{L_\delta} H_L(\bar{s}) \left(\delta + c\frac{d\delta}{d\tau} \right) + d_1 \frac{d\delta}{d\tau} + d_2 \frac{d^2\delta}{d\tau^2} \tag{3}$$

$$C_m = C_{m_\delta} H_m(\bar{s}) \left(\delta + e\frac{d\delta}{d\tau} \right) + f_1 \frac{d\delta}{d\tau} + f_2 \frac{d^2\delta}{d\tau^2} \tag{4}$$

where $H_L(\bar{s})$ and $H_m(\bar{s})$ are transfer function representing the effect of the motion of the control surface on the unsteady lift and pitching moment, respectively. For incompressible flow, $H_L(\bar{s}) = C(\bar{s})$ and $H_m(\bar{s}) = C(\bar{s})$.

The steady-state lift and pitching moment coefficients are functions of the control surface deflection to account for nonlinear behaviors due to flow separation at large deflection angles. They are proposed to be of the form

$$\bar{C}_L = \begin{cases} \bar{C}_{L_\delta}\bar{\delta} & \delta_{ns} \le \bar{\delta} \le \delta_{ps} \\ \bar{C}_{L_\delta^3}\left(\bar{\delta}-\delta_{ps}\right)^3 + \bar{C}_{L_{\delta^2}}\left(\bar{\delta}-\delta_{ps}\right)^2 + \bar{C}_{L_\delta}\left(\bar{\delta}-\delta_{ps}\right) & \bar{\delta} > \delta_{ps} \\ \bar{C}_{L_\delta^3}\left(\bar{\delta}-\delta_{ns}\right)^3 + \bar{C}_{L_{\delta^2}}\left(\bar{\delta}-\delta_{ns}\right)^2 + \bar{C}_{L_\delta}\left(\bar{\delta}-\delta_{ns}\right) & \bar{\delta} < \delta_{ns} \end{cases} \tag{5}$$

$$\bar{C}_m = \begin{cases} \bar{C}_{m_\delta} & \delta_{ns} \le \bar{\delta} \le \delta_{ps} \\ \bar{C}_{m_\delta^3}\left(\bar{\delta}-\delta_{ps}\right)^3 + \bar{C}_{m_{\delta^2}}\left(\bar{\delta}-\delta_{ps}\right)^2 + \bar{C}_{m_\delta}\left(\bar{\delta}-\delta_{ps}\right) & \bar{\delta} > \delta_{ps} \\ \bar{C}_{m_\delta^3}\left(\bar{\delta}-\delta_{ns}\right)^3 + \bar{C}_{m_{\delta^2}}\left(\bar{\delta}-\delta_{ns}\right)^2 + \bar{C}_{m_\delta}\left(\bar{\delta}-\delta_{ps}\right) & \bar{\delta} < \delta_{ns} \end{cases} \tag{6}$$

where δ_{ps} and δ_{ns} denote the control surface deflections where the effect of nonlinear aerodynamics begins to set in for positive and negative deflections, respectively. This model provides a linear response if the control surface deflections are kept sufficiently small to within the linear range corresponding to attached flow at the trailing edge. Beyond the linear range when δ_{ns} and δ_{ps} are exceeded, flow separation occurs. Increasing the control surface deflections cause further flow separation and nonlinearity. The nonlinear effect is described by a cubic polynomial for the lift and pitching moment coefficients.

The steady-state lift and pitching moment control derivatives are obtained by taking the derivatives with respect to the control surface deflection. This results in

$$\bar{C}_{L_{\bar{\delta}}} = \sum_{j=1}^{3} \bar{\sigma}_{j-1}\bar{\delta}^{j-1} \tag{7}$$

$$\bar{C}_{m_{\bar{\delta}}} = \sum_{j=1}^{3} \bar{\eta}_{j-1}\bar{\delta}^{j-1} \tag{8}$$

where

$$\bar{\sigma}_{j-1} = \frac{\partial}{\partial \bar{\delta}^{j-1}} \left(\frac{\partial \bar{C}_L}{\partial \bar{\delta}} \right) \tag{9}$$

$$\bar{\eta}_{j-1} = \frac{\partial}{\partial \bar{\delta}^{j-1}} \left(\frac{\partial \bar{C}_m}{\partial \bar{\delta}} \right) \tag{10}$$

Consider the harmonic motion of the control surface prescribed by

$$\delta = \bar{\delta} + \tilde{\delta} \tag{11}$$

where $\tilde{\delta}(t)$ is the unsteady component of the deflection which is prescribed by

$$\tilde{\delta} = \delta_0 \sin k\tau \tag{12}$$

The steady-state lift and pitching moment coefficients are recovered from the expressions for the unsteady lift and pitching moment coefficients with $\delta = \bar{\delta}$ and $H_L(0) = 1$ and $H_m(0) = 1$. This implies that $C_{L_\delta} = \bar{C}_{L_{\bar{\delta}}}$ and $C_{m_\delta} = C_{m_{\bar{\delta}}}$.

Therefore, we obtain

$$C_{L_\delta} = \sum_{j=1}^{3} \sigma_{j-1} \delta^{j-1} \tag{13}$$

$$C_{m_\delta} = \sum_{j=1}^{3} \eta_{j-1} \delta^{j-1} \tag{14}$$

The unsteady lift and pitching moment coefficients are obtained as

$$\begin{aligned}\tilde{C}_L = C_L - \bar{C}_L &= H_L(\bar{s}) \left(\sum_{j=1}^{3} \sigma_{j-1} \tilde{\delta}^j + c \sum_{j=1}^{3} \sigma_{j-1} \tilde{\delta}^{j-1} \frac{d\tilde{\delta}}{d\tau} \right) + d_1 \frac{d\tilde{\delta}}{d\tau} + d_2 \frac{d^2\tilde{\delta}}{d\tau^2} \\ &= H_L(\bar{s}) \sum_{j=1}^{3} (1 + c\bar{s}) \sigma_{j-1} \tilde{\delta}^j + \left(d_1 \bar{s} + d_2 \bar{s}^2 \right) \tilde{\delta}\end{aligned} \tag{15}$$

$$\begin{aligned}\tilde{C}_m = C_m - \bar{C}_m &= H_m(\bar{s}) \left(\sum_{j=1}^{3} \eta_{j-1} \tilde{\delta}^j + e \sum_{j=1}^{3} \eta_{j-1} \tilde{\delta}^{j-1} \frac{d\tilde{\delta}}{d\tau} \right) + f_0 \tilde{\delta} + f_1 \frac{d\tilde{\delta}}{d\tau} + f_2 \frac{d^2\tilde{\delta}}{d\tau^2} \\ &= H_m(\bar{s}) \sum_{j=1}^{3} (1 + e\bar{s}) \eta_{j-1} \tilde{\delta}^j + \left(f_0 + f_1 \bar{s} + f_2 \bar{s}^2 \right) \tilde{\delta}\end{aligned} \tag{16}$$

The unsteady lift and pitching moment coefficients can be decomposed into the linear and nonlinear terms as

$$\tilde{C}_L = \sum_{j=1}^{3} \tilde{C}_{L_{\tilde{\delta}^j}}(\bar{s}) \tilde{\delta}^j \tag{17}$$

$$\tilde{C}_m = \sum_{j=1}^{3} \tilde{C}_{m_{\tilde{\delta}^j}}(\bar{s}) \tilde{\delta}^j \tag{18}$$

where $C_{L_{\tilde{\delta}^j}}(\bar{s})$ and $C_{m_{\tilde{\delta}^j}}(\bar{s})$ are the dynamic lift and pitching moment control derivatives to be computed from a Fourier series analysis using CFD simulation data. They are expressed as

$$\tilde{C}_{L_{\tilde{\delta}^j}}(\bar{s}) = U_j(k) + iW_j(k) \tag{19}$$

$$\tilde{C}_{m_{\tilde{\delta}^j}}(\bar{s}) = T_j(k) + iV_j(k) \tag{20}$$

where $U_j(k)$, $W_j(k)$, $T_j(k)$, and $V_j(k)$ are the real parts and imaginary parts of $\tilde{C}_{L_{\tilde{\delta}^j}}(\bar{s})$ and $\tilde{C}_{m_{\tilde{\delta}^j}}(\bar{s})$, respectively.

Consider the expression for the unsteady lift coefficient, upon expansion we have

$$\begin{aligned}\tilde{C}_L = &[U_1(k) + iW_1(k)] \delta_0 \sin k\tau + [U_2(k) + iW_2(k)] \delta_0^2 \left(-\frac{1}{2} \cos 2k\tau \right) \\ &+ [U_3(k) + iW_3(k)] \delta_0^3 \left(-\frac{1}{4} \sin 3k\tau + \frac{3}{4} \sin k\tau \right)\end{aligned} \tag{21}$$

The Fourier series coefficients $U_j(k)$ and $W_j(k)$, $j = 1, 2, 3$, are obtained as

$$U_1(k) = \frac{k \int_0^{\frac{2n\pi}{k}} \left(\tilde{C}_L \sin k\tau d\tau + 3\sin 3k\tau\right) d\tau}{n\pi\delta_0} \tag{22}$$

$$W_1(k) = \frac{k \int_0^{\frac{2n\pi}{k}} \tilde{C}_L \left(\cos k\tau d\tau + \cos 3k\tau\right) d\tau}{n\pi\delta_0} \tag{23}$$

$$U_2(k) = -\frac{2k \int_0^{\frac{2n\pi}{k}} \tilde{C}_L \cos 2k\tau d\tau}{n\pi\delta_0^2} \tag{24}$$

$$W_2(k) = \frac{k \int_0^{\frac{2n\pi}{k}} \tilde{C}_L \sin 2k\tau d\tau}{n\pi\delta_0^2} \tag{25}$$

$$U_3(k) = -\frac{4k \int_0^{\frac{2n\pi}{k}} \tilde{C}_L \sin 3k\tau d\tau}{n\pi\delta_0^3} \tag{26}$$

$$W_3(k) = -\frac{4k \int_0^{\frac{2n\pi}{k}} \tilde{C}_L \cos 3k\tau d\tau}{3n\pi\delta_0^3} \tag{27}$$

The Fourier series coefficients $T_j(k)$and $V_j(k)$ are obtained in the same manner.

From the expressions for the unsteady lift and pitching moment coefficients, we have

$$\tilde{C}_L = H_L(\bar{s}) \sum_{j=1}^{3} \left(\sigma_{j-1} + \mu_{j-1}\bar{s}\right) \tilde{\delta}^j + \left(d_1\bar{s} + d_2\bar{s}^2\right) \tilde{\delta} \tag{28}$$

$$\tilde{C}_m = H_m(\bar{s}) \sum_{j=1}^{3} \left(\eta_{j-1} + \kappa_{j-1}\bar{s}\right) \tilde{\delta}^j + \left(f_1\bar{s} + f_2\bar{s}^2\right) \tilde{\delta} \tag{29}$$

where $\mu_j = c\sigma_j$ and $\kappa_j = e\eta_j$.

Hence,

$$\tilde{C}_{L_{\tilde{\delta}^j}}(\bar{s}) = \begin{cases} H_L(\bar{s})(\sigma_0 + \mu_0\bar{s}) + d_1\bar{s} + d_2\bar{s}^2 & j = 1 \\ H_L(\bar{s})\left(\sigma_{j-1} + \mu_{j-1}\bar{s}\right) & j \neq 1 \end{cases} \tag{30}$$

$$\tilde{C}_{m_{\tilde{\delta}^j}}(\bar{s}) = \begin{cases} H_L(\bar{s})(\eta_0 + \kappa_0\bar{s}) + f_1\bar{s} + f_2\bar{s}^2 & j = 1 \\ H_L(\bar{s})\left(\eta_{j-1} + \kappa_{j-1}\bar{s}\right) & j \neq 1 \end{cases} \tag{31}$$

The unsteady aerodynamic transfer function $H_L(\bar{s})$ has a form

$$H_L(\bar{s}) = 1 + \frac{\sum_{j=1}^{m} a_j\bar{s}^j}{\bar{s}^n + \sum_{j=0}^{n-1} b_j\bar{s}^j} \tag{32}$$

where $m \leq n$. The denominator polynomial is also expressed as

$$\bar{s}^n + \sum_{j=0}^{n-1} b_j\bar{s}^j = \Pi_{j=1}^{n}\left(\bar{s} - p_j\right) \tag{33}$$

where p_i, $i = 1, \ldots, n$ are poles of the transfer function $H_L(\bar{s})$ such that $p_j < 0$ for all $j = 1, \ldots, n$. The transfer function $H_m(\bar{s})$ has the same form as $H_L(\bar{s})$.

Since $H_L(0) = 1$ is required for steady-state response, the transfer function $H_L(\bar{s})$ must be equal to 1 and have zero imaginary part at $\bar{s} = 0$. It also must be a stable and proper transfer function. From linear systems theory, a proper transfer function is expressed as a rational fraction with the polynomial in the numerator having the same degree as the degree of the polynomial in the denominator. A stable transfer function has stable poles which are the roots of the polynomial in the denominator. All stable poles must have negative real part.

The selection of the transfer function $H_L(\bar{s})$ is essential in the estimation of the dynamic control derivatives. A good selection of $H_L(\bar{s})$ ensures a goodness of fit of the frequency response data in the frequency domain. The selection of the stable poles are also important. To ensure exponential decay in the response, the stable poles should not be complex as this will result in an amplification at the resonant frequency which is determined by the imaginary part of the poles.

A simple transfer function for $H_L(\bar{s})$ is a second-order transfer function

$$H_L(\bar{s}) = 1 + \frac{a_2\bar{s}^2 + a_1\bar{s}}{\bar{s}^2 + b_1\bar{s} + b_0} \tag{34}$$

which can approximate the Theodorsen's function $C(\bar{s})$ with reasonable accuracy. The order of $H_L(\bar{s})$ can increase to capture better accuracy.

A frequency-domain regression is performed to compute the coefficients of the unsteady lift coefficient. For the regression to have a unique solution, $m = n - 1$. Assuming n is even, then the transfer function $\tilde{C}_{L_{\bar{\delta}j}}(\bar{s})$ can be expressed as

$$\tilde{C}_{L_{\bar{\delta}j}}(\bar{s}) = \frac{N(\bar{s})}{D(\bar{s})} \tag{35}$$

where $N(\bar{s})$ is a polynomial of degree $n+2$ and $D(\bar{s})$ is a polynomial of degree n. The poles are pre-selected to be stable poles. Hence, the polynomial $D(\bar{s})$ is known. The objective of the regression is to estimate the polynomial coefficients of the polynomial $N(\bar{s})$. The polynomials $N(\bar{s})$ and $D(\bar{s})$ are expressed as

$$\begin{aligned} N(\bar{s}) = \sum_{j=0}^{n+2} e_j\bar{s}^j &= \left[e_0 - e_2k^2 + e_4k^4 - \cdots + (-1)^{n/2+1} e_{n+2}k^{n+2}\right] \\ &\quad + i\left[e_1k - e_3k^3 + e_5k^5 - \cdots + (-1)^{n/2} e_{n+1}k^{n+1}\right] \\ &= \sum_{j=0}^{n/2+1} (-1)^j e_{2j}k^{2j} + i\sum_{j=0}^{n/2} (-1)^j e_{2j+1}k^{2j+1} \end{aligned} \tag{36}$$

$$\begin{aligned} D(\bar{s}) = \bar{s}^n + \sum_{j=0}^{n-1} b_j\bar{s}^j &= (-1)^{n/2} k^n + \left[b_0 - b_2k^2 + b_4k^4 - \cdots + (-1)^{n/2-1} b_{n-2}k^{n-2}\right] \\ &\quad + i\left[b_1k - b_3k^3 + b_5k^5 - \cdots + (-1)^{n/2-1} b_{n-1}k^{n-1}\right] \\ &= (-1)^{n/2} k^n + \sum_{j=0}^{n/2-1} (-1)^j b_{2j}k^{2j} + i\sum_{j=0}^{n/2-1} (-1)^j b_{2j+1}k^{2j+1} \end{aligned} \tag{37}$$

The estimation error between the transfer function and the frequency domain data is expressed as

$$\Delta(\bar{s}) = \tilde{C}_{L_{\bar{\delta}j}}(\bar{s}) - [U_j(k) + iW_j(k)] = \frac{N(\bar{s})}{D(\bar{s})} - [U_j(k) + i_jW(k)] \tag{38}$$

The estimation error goes to zero if the magnitude of the numerator of the estimation error is zero. We define an alternative estimation error

$$\varepsilon(\bar{s}) = D(\bar{s})\Delta(\bar{s}) = N(\bar{s}) - D(\bar{s})[U_j(k) + iW_j(k)] \tag{39}$$

Thus, the estimation of the transfer function can be obtained by minimizing the magnitude square of the numerator of the estimation error by the following cost function:

$$\min_{e_j, j=1,\ldots n+2} J = \sum_{l=1}^{N} \frac{1}{2} \|\varepsilon(\bar{s}_l)\|^2 \tag{40}$$

$\varepsilon(\bar{s}_l)$ is separated into the real part and imaginary part as

$$\begin{aligned} \varepsilon(\bar{s}_l) &= \Re(N(k_l)) + i\Im(N(k_l)) - [\Re(D(k_l)) + i\Im(D(k_l))][U_j(k_l) + iW_j(k_l)] \\ &= [\Re(N(k_l)) - \Re(D(k_l))U_j(k_l) + \Im(D(k_l))W_j(k_l)] \\ &\quad + i[\Im(N(k_l)) - \Re(D(k_l))W_j(k_l) - \Im(D(k_j))U(k_j)] \end{aligned} \tag{41}$$

This equation can be written as

$$\varepsilon\left(\bar{s}_l\right)=\boldsymbol{\Theta}^\top\boldsymbol{\Phi}\left(\bar{s}_l\right)-y\left(\bar{s}_l\right) \tag{42}$$

where

$$\boldsymbol{\Theta}=\left[\begin{array}{cccccccc} e_{n+2} & e_{n+1} & e_n & e_{n-1} & \cdots & e_1 & e_0 \end{array}\right]^\top \tag{43}$$

$$\boldsymbol{\Phi}\left(\bar{s}_l\right)=\boldsymbol{\Phi}_R\left(k_l\right)+i\boldsymbol{\Phi}_I\left(k_l\right) \tag{44}$$

$$\boldsymbol{\Phi}_R\left(k_l\right)=\left[\begin{array}{cccccccc} (-1)^{n/2+1}k_l^{n+2} & 0 & (-1)^{n/2}k_l^n & 0 & \cdots & 0 & 1 \end{array}\right]^\top \tag{45}$$

$$\boldsymbol{\Phi}_I\left(k_j\right)=\left[\begin{array}{cccccccc} 0 & (-1)^{n/2}k_l^{n+1} & 0 & (-1)^{n/2-1}k_l^{n-1} & \cdots & k_l & 0 \end{array}\right]^\top \tag{46}$$

$$y\left(\bar{s}_l\right)=y_R\left(k_l\right)+iy_I\left(k_l\right) \tag{47}$$

$$y_R\left(k_l\right)=\Re\left(D\left(k_l\right)\right)U\left(k_l\right)-\Im\left(D\left(k_l\right)\right)W\left(k_l\right) \tag{48}$$

$$y_I\left(k_l\right)=\Re\left(D\left(k_l\right)\right)W\left(k_l\right)+\Im\left(D\left(k_l\right)\right)U\left(k_l\right) \tag{49}$$

The cost function is expressed as

$$\begin{aligned}\min_{\boldsymbol{\Theta}}J&=\sum_{l=1}^{N}\frac{1}{2}\left\|\boldsymbol{\Theta}^\top\boldsymbol{\Phi}\left(\bar{s}_l\right)-y\left(\bar{s}_l\right)\right\|^2\\&=\sum_{l=1}^{N}\frac{1}{2}\left[\left\|\boldsymbol{\Theta}^\top\boldsymbol{\Phi}_R\left(k_l\right)-y_R\left(k_l\right)\right\|^2+\left\|\boldsymbol{\Theta}^\top\boldsymbol{\Phi}_I\left(k_l\right)-y_I\left(k_l\right)\right\|^2\right]\end{aligned} \tag{50}$$

The estimation is performed over a data set of N data points. The standard method for minimization is to obtain the necessary condition. This results in

$$\frac{\partial J}{\partial\boldsymbol{\Theta}}=\sum_{l=1}^{N}\left\{\boldsymbol{\Phi}_R\left(k_l\right)\left[\boldsymbol{\Phi}_R^\top\left(k_l\right)\boldsymbol{\Theta}-y_R\left(k_l\right)\right]+\boldsymbol{\Phi}_I\left(k_l\right)\left[\boldsymbol{\Phi}_I^\top\left(k_l\right)\boldsymbol{\Theta}-y_I\left(k_l\right)\right]\right\}=\mathbf{0} \tag{51}$$

The resulting equations can be cast in a matrix equation of the form

$$\mathbf{A}\boldsymbol{\Theta}=\mathbf{b} \tag{52}$$

where

$$\mathbf{A}=\sum_{l=1}^{N}\left[\boldsymbol{\Phi}_R\left(k_l\right)\boldsymbol{\Phi}_R^\top\left(k_l\right)+\boldsymbol{\Phi}_I\left(k_l\right)\boldsymbol{\Phi}_I^\top\left(k_l\right)\right] \tag{53}$$

$$\mathbf{b}=\sum_{l=1}^{N}\left[\boldsymbol{\Phi}_R\left(k_j\right)y_R\left(k_l\right)+\boldsymbol{\Phi}_I\left(k_l\right)y_I\left(k_l\right)\right] \tag{54}$$

The pre-selected poles are chosen for the regression to be within a reduced frequency range defined by $\max_{j=1,\ldots,n}\left|p_j\right|=rk_{max}$, where r is an integer which can be set to unity as a starting point. The poles are optimized by an exhaustive search method with the values generated by a random function. This is essentially an outer loop optimization process which is defined by

$$\min_{p_{j,j=1,\ldots n}}\min_{\boldsymbol{\Theta}}J\frac{1}{2}\left\|\varepsilon\left(\bar{s}_l\right)\right\|^2 \tag{55}$$

Once the coefficients e_j, $j=1,\ldots,n+2$ and b_j, $j=1,\ldots,n$ are determined, the coefficients a_j of $H_L(\bar{s})$, σ_{j-1}, μ_{j-1}, d_1, and d_2 for $\tilde{C}_{L_{\bar{\delta}}j}(\bar{s})$, $j=1$ are computed next from the solution of nonlinear equations that map the coefficients e_j and b_j to the coefficients a_j, σ_j, c_j. For $j\neq 1$, $e_{n+2}=0$ and $e_{n+1}=0$ since $d_1=0$ and $d_2=0$.

From the regression results, the linear lift dynamic control derivatives are obtained as

$$C_{L_\delta}\left(\bar{s}\right)=H_L\left(\bar{s}\right)\sigma_0 \tag{56}$$

$$C_{L_{\dot{\delta}}}\left(\bar{s}\right)=H_L\left(\bar{s}\right)\mu_0+d_1 \tag{57}$$

$$C_{L_{\ddot{\delta}}}=d_2 \tag{58}$$

The nonlinear lift dynamic control derivatives are obtained as

$$C_{L_{\delta j}}(\bar{s}) = H_L(\bar{s})\,\sigma_{j-1} \tag{59}$$

$$C_{L_{\dot{\delta} j}}(\bar{s}) = H_L(\bar{s})\,\mu_{j-1} \tag{60}$$

for $j = 2,3$. Note that $C_{L_{\dot{\delta} j}}(\bar{s})$ should be interpreted as $\frac{\partial C_L}{\partial\left(\frac{d\left(\delta^j\right)}{dt}\right)}$.

The estimation of the pitch dynamic control derivatives follows the same process as that for the lift dynamic control derivatives. The linear pitching moment dynamic control derivatives are obtained as

$$C_{m_\delta}(\bar{s}) = H_m(\bar{s})\,\eta_0 \tag{61}$$

$$C_{m_{\dot{\delta}}}(\bar{s}) = H_m(\bar{s})\,\kappa_0 + f_1 \tag{62}$$

$$C_{m_{\ddot{\delta}}} = f_2 \tag{63}$$

The nonlinear lift dynamic control derivatives are obtained as

$$C_{m_{\delta j}}(\bar{s}) = H_m(\bar{s})\,\eta_{j-1} \tag{64}$$

$$C_{m_{\dot{\delta} j}}(\bar{s}) = H_m(\bar{s})\,\kappa_{j-1} \tag{65}$$

for $j = 2,3$.

A. Control Derivatives Due to Unsteady Drag

Regarding the drag coefficient which is nonlinear with respect to the control surface deflection, the unsteady drag can be modeled as a function of the unsteady lift coefficient according to the parabolic drag polar model.[4] Since the nonlinear lift coefficient is described by a cubic polynomial, the unsteady drag coefficient is expressed as a 6^{th}-degree polynomial.

$$\tilde{C}_D = \frac{\partial \tilde{C}_D}{\partial \tilde{C}_L}(\bar{s})\,\tilde{C}_L + \frac{\partial \tilde{C}_D}{\partial \tilde{C}_L^2}(\bar{s})\,\tilde{C}_L^2 = \sum_{j=1}^{6} \tilde{C}_{D_{\tilde{\delta} j}}(\bar{s})\,\tilde{\delta}^j \tag{66}$$

where $\tilde{C}_{D_{\tilde{\delta} j}}(\bar{s})$, $i = 1,\ldots,6$, are the drag dynamic control derivative expressed as

$$\tilde{C}_{D_{\tilde{\delta} j(\bar{s})}} = Q_j(k) + iS_j(k) \tag{67}$$

where $Q_j(k)$ and $S_j(k)$ are the real parts and imaginary parts of $\tilde{C}_{D_{\tilde{\delta} j}}(\bar{s})$ and $\frac{\partial \tilde{C}_D}{\partial \tilde{C}_L^2}(\bar{s})$ to be computed from a Fourier series analysis of CFD simulation data.

Upon expansion, the unsteady drag coefficient is expressed as

$$\begin{aligned}
\tilde{C}_D = {} & [Q_1(k) + iS_1(k)]\,\delta_0 \sin k\tau + [Q_2(k) + iS_2(k)]\,\delta_0^2\left(-\frac{1}{2}\cos 2k\tau\right) \\
& + [Q_3(k) + iS_3(k)]\,\delta_0^3\left(-\frac{1}{4}\sin 3k\tau + \frac{3}{4}\sin k\tau\right) \\
& + [Q_4(k) + iS_4(k)]\,\delta_0^4\left(\frac{1}{8}\cos 4k\tau - \frac{1}{2}\cos 2k\tau\right) \\
& + [Q_5(k) + iS_5(k)]\,\delta_0^5\left(\frac{1}{16}\sin 5k\tau - \frac{5}{16}\sin 3k\tau + \frac{5}{8}\sin k\tau\right) \\
& + [Q_6(k) + iS_6(k)]\,\delta_0^6\left(-\frac{1}{32}\cos 6k\tau + \frac{3}{16}\cos 4k\tau - \frac{15}{32}\cos 2k\tau\right)
\end{aligned} \tag{68}$$

From the Fourier series analysis, $Q_j(k)$ and $S_j(k)$ are obtained as

$$Q_1(k) = \frac{k \int_0^{\frac{2n\pi}{k}} \tilde{C}_D (\sin k\tau + 3\sin 3k\tau + 5\sin 5k\tau)\, d\tau}{n\pi\delta_0} \tag{69}$$

$$S_1(k) = \frac{k \int_0^{\frac{2n\pi}{k}} \tilde{C}_D (\cos k\tau + \cos 3k\tau + \cos 5k\tau)\, d\tau}{n\pi\delta_0} \tag{70}$$

$$Q_2(k) = \frac{-2k \int_0^{\frac{2n\pi}{k}} \tilde{C}_D (\cos 2k\tau + 4\cos 4k\tau + 9\cos 6k\tau)\, d\tau}{n\pi\delta_0^2} \tag{71}$$

$$S_2(k) = \frac{k \int_0^{\frac{2n\pi}{k}} \tilde{C}_D (\sin 2k\tau + 2\sin 4k\tau + 3\sin 6k\tau)\, d\tau}{n\pi\delta_0^2} \tag{72}$$

$$Q_3(k) = \frac{-4k \int_0^{\frac{2n\pi}{k}} \tilde{C}_D (\sin 3k\tau + 5\sin 5k\tau)\, d\tau}{n\pi\delta_0^3} \tag{73}$$

$$S_3(k) = \frac{-4k \int_0^{\frac{2n\pi}{k}} \tilde{C}_D (\cos 3k\tau + 3\cos 5k\tau)\, d\tau}{3n\pi\delta_0^3} \tag{74}$$

$$Q_4(k) = \frac{8k \int_0^{\frac{2n\pi}{k}} \tilde{C}_D (\cos 4k\tau + 6\cos 6k\tau)\, d\tau}{n\pi\delta_0^4} \tag{75}$$

$$S_4(k) = \frac{-2k \int_0^{\frac{2n\pi}{k}} \tilde{C}_D (\sin 4k\tau + 4\sin 6k\tau)\, d\tau}{n\pi\delta_0^4} \tag{76}$$

$$Q_5(k) = \frac{16k \int_0^{\frac{2n\pi}{k}} \tilde{C}_D \sin 5k\tau d\tau}{n\pi\delta_0^5} \tag{77}$$

$$S_5(k) = \frac{16k \int_0^{\frac{2n\pi}{k}} \tilde{C}_D \cos 5k\tau d\tau}{5n\pi\delta_0^5} \tag{78}$$

$$Q_6(k) = \frac{-32k \int_0^{\frac{2n\pi}{k}} \tilde{C}_D \cos 6k\tau d\tau}{n\pi\delta_0^6} \tag{79}$$

$$S_6(k) = \frac{16k \int_0^{\frac{2n\pi}{k}} \tilde{C}_D \sin 6k\tau d\tau}{3n\pi\delta_0^6} \tag{80}$$

A frequency-domain regression is performed to estimate the dynamic drag control derivatives in the same manner as the estimation for the lift dynamic control derivatives. The linear drag dynamic control derivatives are obtained as

$$C_{D_\delta}(\bar{s}) = H_D(\bar{s})\gamma_0 \tag{81}$$

$$C_{D_{\dot{\delta}}}(\bar{s}) = H_D(\bar{s})\upsilon_0 + g_1 \tag{82}$$

$$C_{L_{\ddot{\delta}}} = g_2 \tag{83}$$

The nonlinear drag dynamic control derivatives are are obtained as

$$C_{D_{\delta^j}}(\bar{s}) = H_D(\bar{s})\gamma_{j-1} \tag{84}$$

$$C_{D_{\dot{\delta}^j}}(\bar{s}) = H_D(\bar{s})\upsilon_{j-1} \tag{85}$$

for $j = 2, \ldots, 6$.

III. Determination of Dynamic Control Derivatives of Transonic Truss-Braced Wing

The dynamic control derivative estimation method is applied to the Mach 0.8 TTBW to illustrate the procedure. Figure 2 illustrates control surface layout for the Mach 0.8 TTBW.[7]

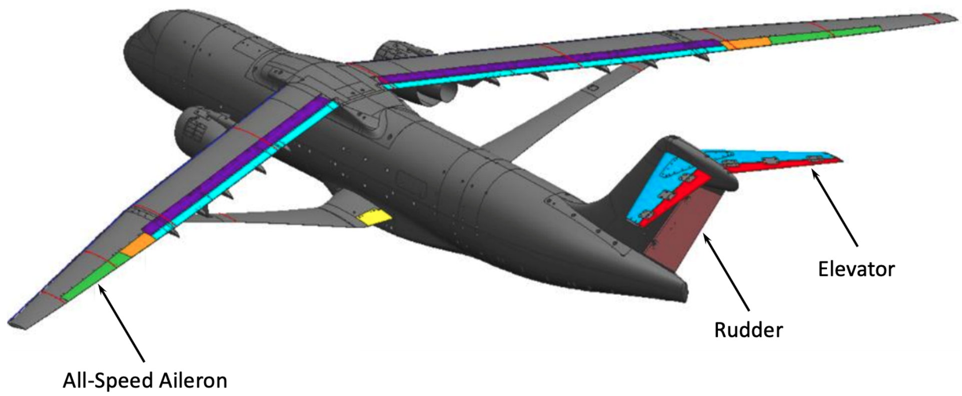

Figure 2. Control Surface Layout of Mach 0.8 Transonic Truss Braced-Wing

A series of unsteady RANS CFD simulations of the control surface oscillations of the elevator of the Mach 0.8 TTBW is conducted in FUN3D.[8] The individual elevator control surfaces are modeled as a single control surface in symmetric deflections. The FUN3D tetrahedral prism mesh has about 96 million nodes. The Roe's flux-difference splitting scheme and the Spalart-Allmaras turbulence model are used in the simulations. An optimized second-order backward finite-difference scheme is used in the time integration. The aircraft is trimmed with the horizontal tail incidence of $-0.75°$ at the design lift coefficient $C_L = 0.695$ and an altitude of 46,716 ft corresponding to the mid-cruise gross weight of 130,486 lbs for the Mach 0.8 TTBW.

A. Elevator Dynamic Control Derivative Estimation

The elevator control surface oscillations are simulated with four different amplitudes of 0.1°, 1°, and 10°, each at three reduced frequencies $k = 0.02$, 0.1, and 0.2. In addition, steady state simulations corresponding to $k = 0$ are also performed.

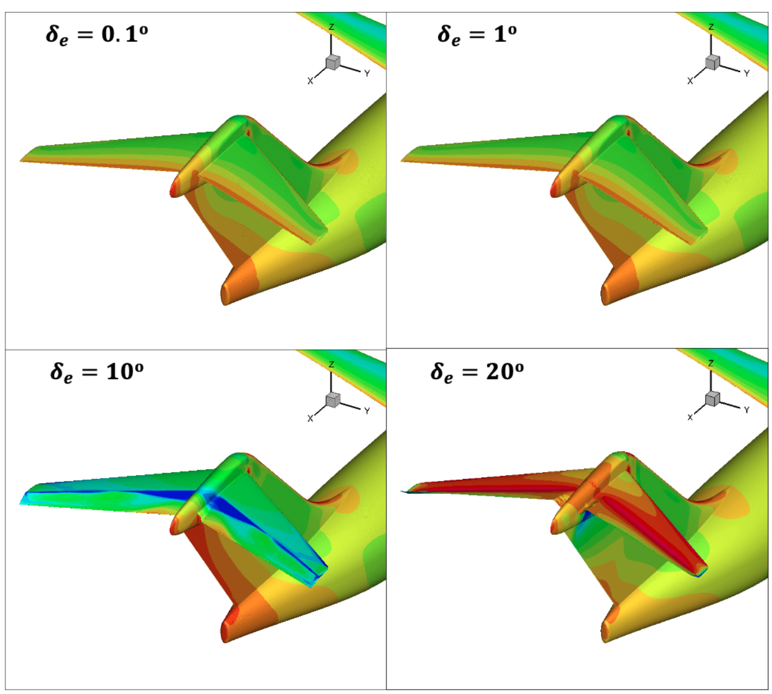

Figure 3. Instantaneous Elevator Control Surface Pressure Contour

Figure 3 is an instantaneous elevator control surface pressure contour plot for $k = 0.2$. The flow over the horizontal tail is seen to be entirely subsonic for small elevator deflections of about 1° or less. Shock-induced boundary layer separation at the hinge line is observed when the elevator deflection is greater than 10°. Figure 4 shows the massive flow separation on the upper surface starting at the hinge line with the elevator deflection of 20°.

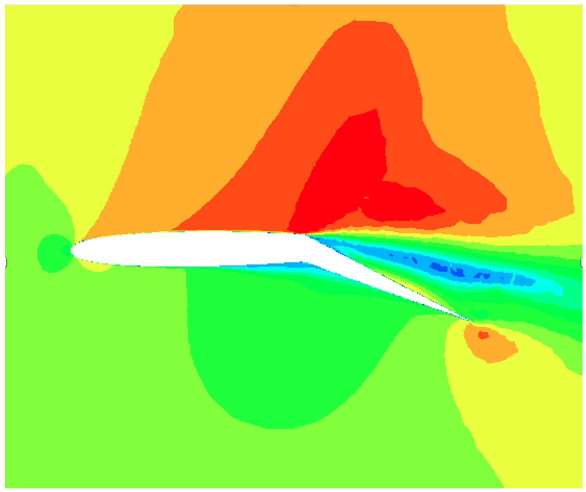

Figure 4. Flow Separation with Elevator Deflection at 20°

The plots of the unsteady lift and pitching moment coefficients versus the elevator control surface deflection for an amplitude of 20° are shown in Figs. 5(a) and (b), respectively. The plots of the approximate lift and pitching coefficients computed by the Fourier series using the first three harmonics are also shown. The Fourier series approximation agrees well with the simulation data. As can be seen, the data shows significant nonlinearity. A linear response would appear as an elliptical curve. The mean response is a median line line passing through the curve. As the reduced frequency increases, the control effectiveness decreases.

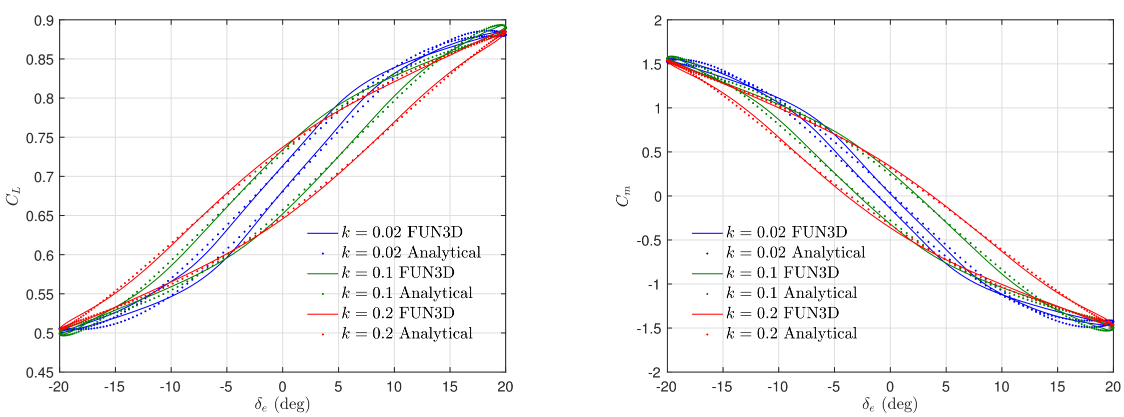

(a) C_L vs. $\tilde{\delta}_e$ (b) C_m vs. $\tilde{\delta}_e$

Figure 5. Lift and Pitching Moment Coefficients vs. Elevator Deflection for 20° **Amplitude**

The plots of the unsteady drag coefficient versus the elevator control surface deflection for an amplitude of 20° are shown in Figs. 6(a) and (b), respectively. The plot of the drag coefficients computed by the Fourier series using the first six harmonics is shown in Figure 6(a). The even harmonics contribute more significantly to the drag coefficient than the odd harmonics above the first harmonics. The plot of the drag coefficients computed by the Fourier series with the third and fifth harmonics removed is shown in Figure 6(a). Both Fourier series approximations show good agreement with the simulation data. This suggests that the nonlinear drag dynamic control derivatives $\tilde{C}_{D_{\tilde{\delta}^3}(\bar{s})}$ and

$\tilde{C}_{D_{\tilde{\delta}^5}(\bar{s})}$ are less important and therefore could be neglected.

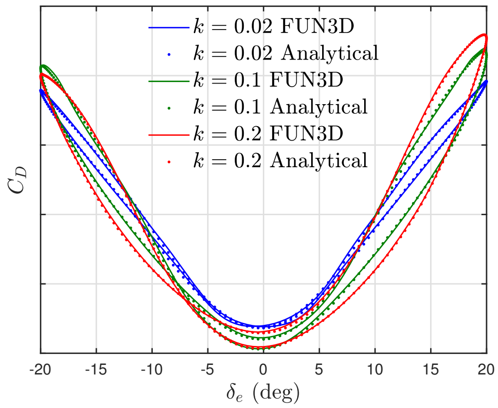

(a) C_D vs. $\tilde{\delta}_e$ with all 6 Harmonics

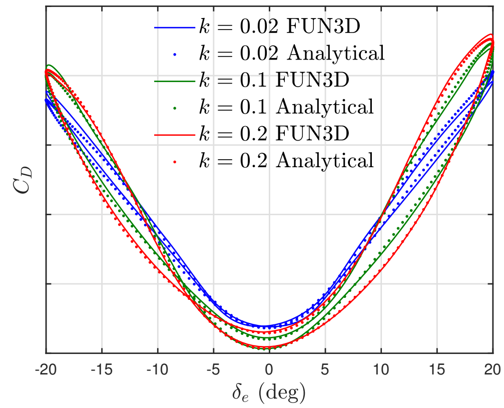

(b) C_D vs. $\tilde{\delta}_e$ without 3rd and 5th Harmonics

Figure 6. Drag Coefficient vs. Elevator Deflection for 20° Amplitude

1. Lift Dynamic Control Derivative Estimation

The frequency-domain regression is performed for the lift and pitching moment coefficients. Figure 7 shows the regression of the linear lift dynamic control derivative $\tilde{C}_{L_{\tilde{\delta}_e}}(\bar{s})$ for the elevator. The estimated lift dynamic control derivative $\tilde{C}_{L_{\tilde{\delta}_e}}(\bar{s})$ is obtained as

$$\tilde{C}_{L_{\tilde{\delta}_e}}(\bar{s}) = \left(1 + \frac{0.4167\bar{s}}{\bar{s}^2 + 0.5802\bar{s} + 0.0753}\right)(0.8648 + 7.7427\bar{s}) - 14.370\bar{s} + 12.791\bar{s}^2$$

The individual dynamic control derivatives are obtained from $\tilde{C}_{L_{\tilde{\delta}_e}}(\bar{s})$ as

$$C_{L_{\delta_e}}(\bar{s}) = \left(1 + \frac{0.4167\bar{s}}{\bar{s}^2 + 0.5802\bar{s} + 0.0753}\right)0.8648$$

$$C_{L_{\dot{\delta}_e}}(\bar{s}) = \left(1 + \frac{0.4167\bar{s}}{\bar{s}^2 + 0.5802\bar{s} + 0.0753}\right)7.7427 - 14.370$$

$$C_{L_{\ddot{\delta}_e}} = 12.791$$

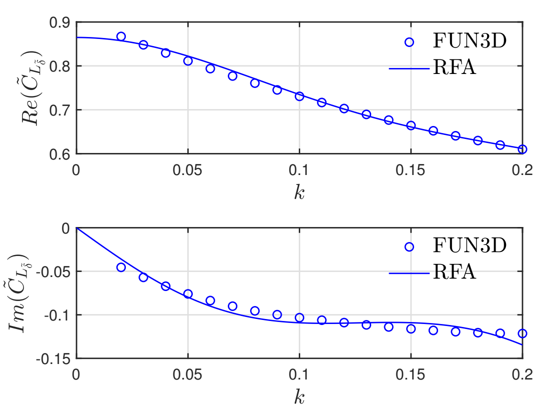

Figure 7. Frequency-Domain Regression of $\tilde{C}_{L_{\tilde{\delta}_e}}$

Figure 8 shows the regression of the nonlinear lift dynamic control derivative $\tilde{C}_{L_{\tilde{\delta}_e^2}}$. The estimated lift dynamic control derivative $\tilde{C}_{L_{\tilde{\delta}_e^2}}(\bar{s})$ is obtained as

$$\tilde{C}_{L_{\tilde{\delta}_e^2}}(\bar{s}) = \left(1 + \frac{2.144\bar{s}^4 - 0.4387\bar{s}^3 - 0.1306\bar{s}^2 - 0.0227\bar{s}}{\bar{s}^4 + 0.6907\bar{s}^3 + 0.1782\bar{s}^2 + 0.0204\bar{s} + 8.6896 \cdot 10^{-4}}\right)(-0.0298 - 0.0877\bar{s})$$

The individual dynamic control derivatives are obtained from $\tilde{C}_{L_{\tilde{\delta}_e^2}}(\bar{s})$ as

$$C_{L_{\delta_e^2}}(\bar{s}) = \left(1 + \frac{2.144\bar{s}^4 - 0.4387\bar{s}^3 - 0.1306\bar{s}^2 - 0.0227\bar{s}}{\bar{s}^4 + 0.6907\bar{s}^3 + 0.1782\bar{s}^2 + 0.0204\bar{s} + 8.6896 \cdot 10^{-4}}\right)(-0.0298)$$

$$C_{L_{\delta_e^2}}(\bar{s}) = \left(1 + \frac{2.144\bar{s}^4 - 0.4387\bar{s}^3 - 0.1306\bar{s}^2 - 0.0227\bar{s}}{\bar{s}^4 + 0.6907\bar{s}^3 + 0.1782\bar{s}^2 + 0.0204\bar{s} + 8.6896 \cdot 10^{-4}}\right)(-0.0877)$$

The magnitude of the dynamic control derivative $\tilde{C}_{L_{\tilde{\delta}_e^2}}(\bar{s})$ is relatively small compared to $\tilde{C}_{L_{\tilde{\delta}_e}}(\bar{s})$.

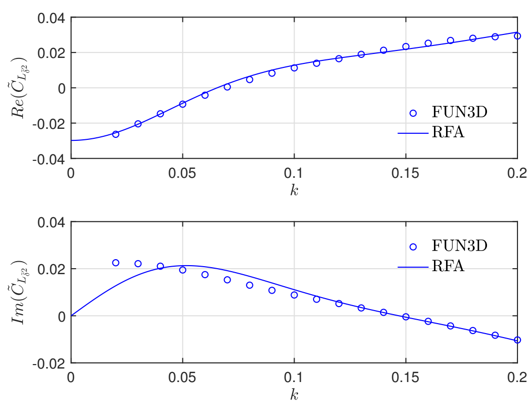

Figure 8. Frequency-Domain Regression of $\tilde{C}_{L_{\tilde{\delta}_e^2}}$

Figure 9 shows the regression of the nonlinear lift dynamic control derivative $\tilde{C}_{L_{\tilde{\delta}_e^3}}$. The estimated lift dynamic control derivative $\tilde{C}_{L_{\tilde{\delta}_e^3}}(\bar{s})$ is obtained as

$$\tilde{C}_{L_{\tilde{\delta}_e^3}}(\bar{s}) = \left(1 + \frac{4209.9\bar{s}^4 - 50.527\bar{s}^3 + 245.09\bar{s}^2 - 16.473\bar{s}}{\bar{s}^4 + 6.1648\bar{s}^3 + 14.222\bar{s}^2 + 14.555\bar{s} + 5.5755}\right)(-2.6160 + 0.5239\bar{s})$$

The individual dynamic control derivatives are obtained from $\tilde{C}_{L_{\tilde{\delta}_e^3}}(\bar{s})$ as

$$C_{L_{\delta_e^3}}(\bar{s}) = \left(1 + \frac{4209.9\bar{s}^4 - 50.527\bar{s}^3 + 245.09\bar{s}^2 - 16.473\bar{s}}{\bar{s}^4 + 6.1648\bar{s}^3 + 14.222\bar{s}^2 + 14.555\bar{s} + 5.5755}\right)(-2.6160)$$

$$C_{L_{\dot{\delta}_e^3}}(\bar{s}) = \left(1 + \frac{4209.9\bar{s}^4 - 50.527\bar{s}^3 + 245.09\bar{s}^2 - 16.473\bar{s}}{\bar{s}^4 + 6.1648\bar{s}^3 + 14.222\bar{s}^2 + 14.555\bar{s} + 5.5755}\right)0.5239$$

The dynamic control derivative $\tilde{C}_{L_{\tilde{\delta}_e^3}}(\bar{s})$ is significant as its magnitude is larger than that of $\tilde{C}_{L_{\tilde{\delta}_e}}(\bar{s})$. The estimation of the imaginary part which is related to the phase information has a discrepancy at high frequencies.

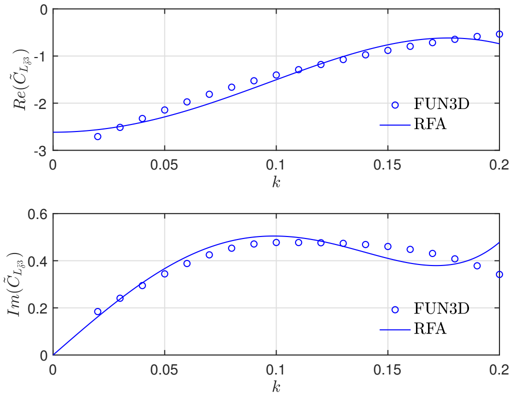

Figure 9. Frequency-Domain Regression of $\tilde{C}_{L_{\tilde{\delta}_e^3}}$

2. *Pitching Moment Dynamic Control Derivative Estimation*

Figure 10 shows the regression of the linear pitching moment dynamic control derivative $\tilde{C}_{m_{\tilde{\delta}_e}}$. The estimated pitching moment dynamic control derivative $\tilde{C}_{m_{\tilde{\delta}_e}}(\bar{s})$ is obtained as

$$\tilde{C}_{m_{\tilde{\delta}_e}}(\bar{s}) = \left(1 + \frac{3.9627\bar{s}}{\bar{s}^2 + 0.7981\bar{s} + 0.1592}\right)(-6.7936 - 29.766\bar{s}) + 210.64\bar{s} - 232.74\bar{s}^2$$

The individual dynamic control derivatives are obtained from $\tilde{C}_{m_{\tilde{\delta}_e}}(\bar{s})$ as

$$C_{m_{\delta_e}}(\bar{s}) = \left(1 + \frac{3.9627\bar{s}}{\bar{s}^2 + 0.7981\bar{s} + 0.1592}\right)(-6.7936)$$

$$C_{m_{\dot{\delta}_e}}(\bar{s}) = \left(1 + \frac{3.9627\bar{s}}{\bar{s}^2 + 0.7981\bar{s} + 0.1592}\right)(-29.766) + 210.64$$

$$C_{m_{\ddot{\delta}_e}} = -232.74$$

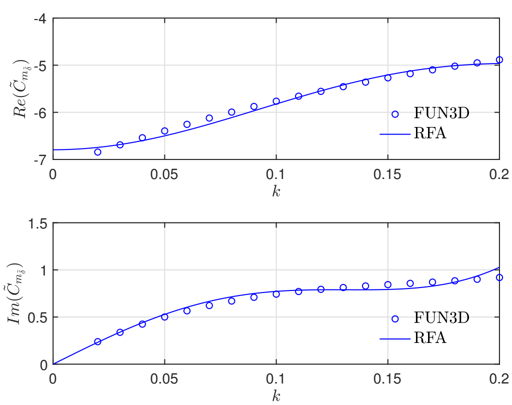

Figure 10. Frequency-Domain Regression of $\tilde{C}_{m_{\tilde{\delta}_e}}$

Figure 11 shows the regression of the nonlinear pitching moment dynamic control derivative $\tilde{C}_{m_{\tilde{\delta}_e^2}}$. The estimated pitching moment dynamic control derivative $\tilde{C}_{m_{\tilde{\delta}_e^2}}(\bar{s})$ is obtained as

$$\tilde{C}_{m_{\tilde{\delta}_e^2}}(\bar{s}) = \left(1 + \frac{3472.1\bar{s}^4 - 1939.5\bar{s}^3 + 1839.5\bar{s}^2 - 11.753\bar{s}}{\bar{s}^4 + 5.9503\bar{s}^3 + 13.166\bar{s}^2 + 12.837\bar{s} + 3.6303}\right)(0.7287 + 0.1098\bar{s})$$

The individual dynamic control derivatives are obtained from $\tilde{C}_{m_{\tilde{\delta}_e^2}}(\bar{s})$ as

$$C_{m_{\delta_e^2}}(\bar{s}) = \left(1 + \frac{3472.1\bar{s}^4 - 1939.5\bar{s}^3 + 1839.5\bar{s}^2 - 11.753\bar{s}}{\bar{s}^4 + 5.9503\bar{s}^3 + 13.166\bar{s}^2 + 12.837\bar{s} + 3.6303}\right)0.7287$$

$$C_{m_{\dot{\delta}_e^2}}(\bar{s}) = \left(1 + \frac{3472.1\bar{s}^4 - 1939.5\bar{s}^3 + 1839.5\bar{s}^2 - 11.753\bar{s}}{\bar{s}^4 + 5.9503\bar{s}^3 + 13.166\bar{s}^2 + 12.837\bar{s} + 3.6303}\right)0.1098$$

The magnitude of the dynamic control derivative $\tilde{C}_{m_{\tilde{\delta}_e^2}}(\bar{s})$ is relatively small compared to $\tilde{C}_{m_{\tilde{\delta}_e}}(\bar{s})$. The regression does not match the data well. This may indicate that a higher-order transfer function may be needed to increase the accuracy of the regression.

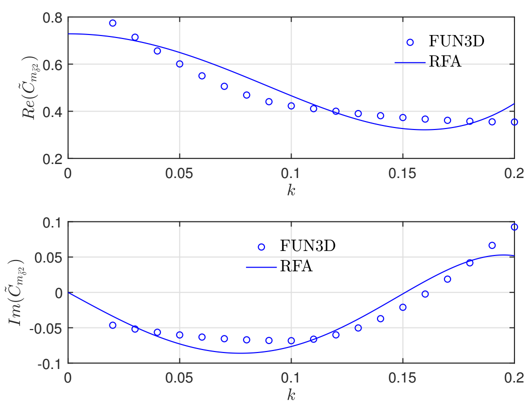

Figure 11. Frequency-Domain Regression of $\tilde{C}_{m_{\tilde{\delta}_e^2}}$

Figure 12 shows the regression of the nonlinear pitching moment dynamic control derivative $\tilde{C}_{m_{\tilde{\delta}_e^3}}$. The estimated pitching moment dynamic control derivative $\tilde{C}_{m_{\tilde{\delta}_e^3}}(\bar{s})$ is obtained as

$$\tilde{C}_{m_{\tilde{\delta}_e^3}}(\bar{s}) = \left(1 + \frac{4644.1\bar{s}^4 - 52.146\bar{s}^3 + 269.59\bar{s}^2 - 17.247\bar{s}}{\bar{s}^4 + 6.3285\bar{s}^3 + 15.018\bar{s}^2 + 15.839\bar{s} + 6.1153}\right)(20.779 - 7.8723\bar{s})$$

The individual dynamic control derivatives are obtained from $\tilde{C}_{m_{\tilde{\delta}_e^3}}(\bar{s})$ as

$$C_{m_{\delta_e^3}}(\bar{s}) = \left(1 + \frac{4644.1\bar{s}^4 - 52.146\bar{s}^3 + 269.59\bar{s}^2 - 17.247\bar{s}}{\bar{s}^4 + 6.3285\bar{s}^3 + 15.018\bar{s}^2 + 15.839\bar{s} + 6.1153}\right)20.779$$

$$C_{m_{\dot{\delta}_e^3}}(\bar{s}) = \left(1 + \frac{4644.1\bar{s}^4 - 52.146\bar{s}^3 + 269.59\bar{s}^2 - 17.247\bar{s}}{\bar{s}^4 + 6.3285\bar{s}^3 + 15.018\bar{s}^2 + 15.839\bar{s} + 6.1153}\right)(-7.8723)$$

The magnitude of $\tilde{C}_{m_{\tilde{\delta}_e^3}}(\bar{s})$ is about three times larger than that of $\tilde{C}_{m_{\tilde{\delta}_e}}(\bar{s})$, thereby contributing significantly to the nonlinearity in the pitching moment coefficient.

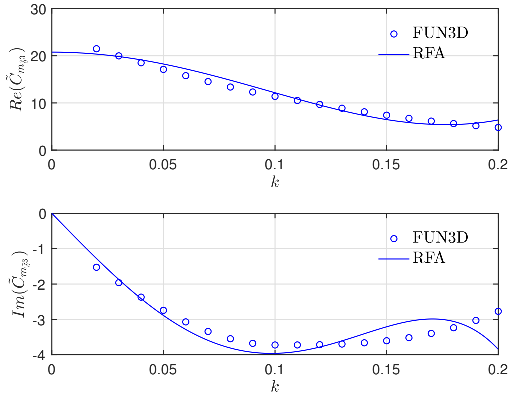

Figure 12. Frequency-Domain Regression of $\tilde{C}_{m_{\tilde{\delta}_e^3}}$

3. Drag Dynamic Control Derivative Estimation

Figure 13 shows the regression of the linear drag dynamic control derivative $\tilde{C}_{D_{\tilde{\delta}_e}}$. The estimated drag dynamic control derivative $\tilde{C}_{D_{\tilde{\delta}_e}}(\bar{s})$ is obtained as

$$\tilde{C}_{D_{\tilde{\delta}_e}}(\bar{s}) = \left(1 + \frac{345.99\bar{s}}{\bar{s}^2 + 2.8129\bar{s} + 1.4082}\right)(0.005842 + 0.009459\bar{s}) - 1.4254\bar{s} + 0.5459\bar{s}^2$$

The individual dynamic control derivatives are obtained from $\tilde{C}_{D_{\tilde{\delta}_e}}(\bar{s})$ as

$$C_{D_{\delta_e}}(\bar{s}) = \left(1 + \frac{345.99\bar{s}}{\bar{s}^2 + 2.8129\bar{s} + 1.4082}\right)0.005842$$

$$C_{D_{\dot{\delta}_e}}(\bar{s}) = \left(1 + \frac{345.99\bar{s}}{\bar{s}^2 + 2.8129\bar{s} + 1.4082}\right)0.009459 - 1.4254$$

$$C_{m_{\ddot{\delta}_e}} = 0.5459$$

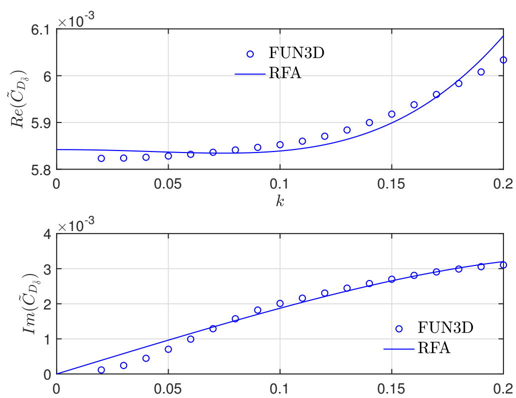

Figure 13. Frequency-Domain Regression of $\tilde{C}_{D_{\tilde{\delta}_e}}$

Figure 14 shows the regression of the nonlinear drag dynamic control derivative $\tilde{C}_{D_{\tilde{\delta}_e^2}}$. The estimated drag dynamic control derivative $\tilde{C}_{D_{\tilde{\delta}_e^2}}(\bar{s})$ is obtained as

$$\tilde{C}_{D_{\tilde{\delta}_e^2}}(\bar{s}) = \left(1 + \frac{2014.2\bar{s}^4 + 1966.7\bar{s}^3 + 567.45\bar{s}^2 + 111.46\bar{s}}{\bar{s}^4 + 9.8326\bar{s}^3 + 36.120\bar{s}^2 + 58.768\bar{s} + 35.741}\right)(0.5867 - 1.8545\bar{s})$$

The individual dynamic control derivatives are obtained from $\tilde{C}_{D_{\tilde{\delta}_e^2}}(\bar{s})$ as

$$C_{D_{\delta_e^2}}(\bar{s}) = \left(1 + \frac{2014.2\bar{s}^4 + 1966.7\bar{s}^3 + 567.45\bar{s}^2 + 111.46\bar{s}}{\bar{s}^4 + 9.8326\bar{s}^3 + 36.120\bar{s}^2 + 58.768\bar{s} + 35.741}\right)0.5867$$

$$C_{D_{\delta_e^2}}(\bar{s}) = \left(1 + \frac{2014.2\bar{s}^4 + 1966.7\bar{s}^3 + 567.45\bar{s}^2 + 111.46\bar{s}}{\bar{s}^4 + 9.8326\bar{s}^3 + 36.120\bar{s}^2 + 58.768\bar{s} + 35.741}\right)(-1.8545)$$

The magnitude of $\tilde{C}_{D_{\tilde{\delta}_e^2}}(\bar{s})$ is about 10 times larger than that of $\tilde{C}_{D_{\tilde{\delta}_e}}(\bar{s})$ which indicates that the quadratic drag contribution is larger than the linear contribution.

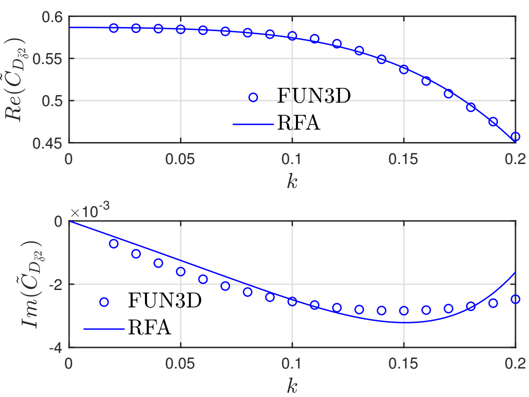

Figure 14. Frequency-Domain Regression of $\tilde{C}_{D_{\tilde{\delta}_e^2}}$

Figure 15 shows the regression of the nonlinear drag dynamic control derivative $\tilde{C}_{D_{\tilde{\delta}_e^3}}$. The estimated drag dynamic control derivative $\tilde{C}_{D_{\tilde{\delta}_e^3}}(\bar{s})$ is obtained as

$$\tilde{C}_{D_{\tilde{\delta}_e^3}}(\bar{s}) = \left(1 + \frac{3.0626\bar{s}^4 - 0.1082\bar{s}^3 - 0.1840\bar{s}^2 - 0.03445\bar{s}}{\bar{s}^4 + 1.1435\bar{s}^3 + 0.4869\bar{s}^2 + 0.09145\bar{s} + 0.006388 \cdot 10^{-4}}\right)(-0.04918 - 0.1439\bar{s})$$

The individual dynamic control derivatives are obtained from $\tilde{C}_{D_{\tilde{\delta}_e^3}}(\bar{s})$ as

$$C_{D_{\delta_e^3}}(\bar{s}) = \left(1 + \frac{3.0626\bar{s}^4 - 0.1082\bar{s}^3 - 0.1840\bar{s}^2 - 0.03445\bar{s}}{\bar{s}^4 + 1.1435\bar{s}^3 + 0.4869\bar{s}^2 + 0.09145\bar{s} + 0.006388 \cdot 10^{-4}}\right)(-0.04918)$$

$$C_{D_{\delta_e^3}}(\bar{s}) = \left(1 + \frac{3.0626\bar{s}^4 - 0.1082\bar{s}^3 - 0.1840\bar{s}^2 - 0.03445\bar{s}}{\bar{s}^4 + 1.1435\bar{s}^3 + 0.4869\bar{s}^2 + 0.09145\bar{s} + 0.006388 \cdot 10^{-4}}\right)(-0.1439)$$

The magnitude of $\tilde{C}_{D_{\tilde{\delta}_e^3}}(\bar{s})$ is quite small compared to that of $\tilde{C}_{D_{\tilde{\delta}_e}}(\bar{s})$ which indicates that the cubic drag contribution could be neglected.

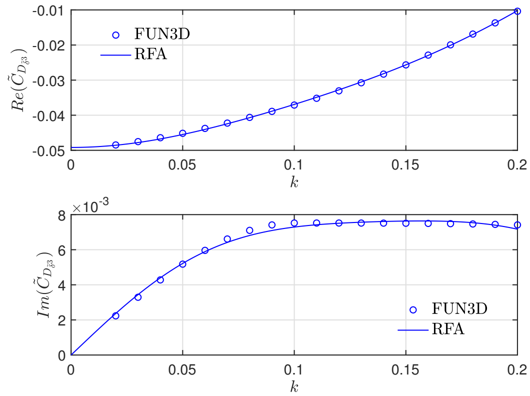

Figure 15. Frequency-Domain Regression of $\tilde{C}_{D_{\tilde{\delta}_e^3}}$

Figure 16 shows the regression of the nonlinear drag dynamic control derivative $\tilde{C}_{D_{\tilde{\delta}_e^4}}$. The estimated drag dynamic control derivative $\tilde{C}_{D_{\tilde{\delta}_e^4}}(\bar{s})$ is obtained as

$$\tilde{C}_{D_{\tilde{\delta}_e^4}}(\bar{s}) = \left(1 + \frac{2.5122\bar{s}^4 - 0.06316\bar{s}^3 - 0.2550\bar{s}^2 - 0.05587\bar{s}}{\bar{s}^4 + 1.2347\bar{s}^3 + 0.5706\bar{s}^2 + 0.1170\bar{s} + 0.008976}\right)(-4.2855 - 22.267\bar{s})$$

The individual dynamic control derivatives are obtained from $\tilde{C}_{D_{\tilde{\delta}_e^4}}(\bar{s})$ as

$$C_{D_{\tilde{\delta}_e^4}}(\bar{s}) = \left(1 + \frac{2.5122\bar{s}^4 - 0.06316\bar{s}^3 - 0.2550\bar{s}^2 - 0.05587\bar{s}}{\bar{s}^4 + 1.2347\bar{s}^3 + 0.5706\bar{s}^2 + 0.1170\bar{s} + 0.008976}\right)(-4.2855)$$

$$C_{D_{\dot{\tilde{\delta}}_e^4}}(\bar{s}) = \left(1 + \frac{2.5122\bar{s}^4 - 0.06316\bar{s}^3 - 0.2550\bar{s}^2 - 0.05587\bar{s}}{\bar{s}^4 + 1.2347\bar{s}^3 + 0.5706\bar{s}^2 + 0.1170\bar{s} + 0.008976}\right)(-22.267)$$

The magnitude of $\tilde{C}_{D_{\tilde{\delta}_e^4}}(\bar{s})$ is larger than that of $\tilde{C}_{D_{\tilde{\delta}_e^2}}(\bar{s})$, but the quadratic drag contribution is larger than the quartic contribution when the deflection is taken into account.

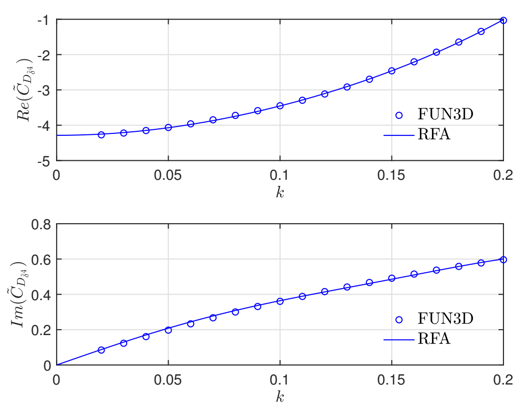

Figure 16. Frequency-Domain Regression of $\tilde{C}_{D_{\tilde{\delta}_e^4}}$

Figure 17 shows the regression of the nonlinear drag dynamic control derivative $\tilde{C}_{D_{\tilde{\delta}_e^5}}$. The estimated drag dynamic control derivative $\tilde{C}_{D_{\tilde{\delta}_e^5}}(\bar{s})$ is obtained as

$$\tilde{C}_{D_{\tilde{\delta}_e^5}}(\bar{s}) = \left(1 + \frac{79374\bar{s}^4 - 5092.5\bar{s}^3 + 1905.3\bar{s}^2 - 187.45\bar{s}}{\bar{s}^4 + 11.255\bar{s}^3 + 47.180\bar{s}^2 + 87.237\bar{s} + 59.977}\right)(0.1244 - 0.01161\bar{s})$$

The individual dynamic control derivatives are obtained from $\tilde{C}_{D_{\tilde{\delta}_e^5}}(\bar{s})$ as

$$C_{D_{\delta_e^5}}(\bar{s}) = \left(1 + \frac{79374\bar{s}^4 - 5092.5\bar{s}^3 + 1905.3\bar{s}^2 - 187.45\bar{s}}{\bar{s}^4 + 11.255\bar{s}^3 + 47.180\bar{s}^2 + 87.237\bar{s} + 59.977}\right)0.1244$$

$$C_{D_{\dot{\delta}_e^5}}(\bar{s}) = \left(1 + \frac{79374\bar{s}^4 - 5092.5\bar{s}^3 + 1905.3\bar{s}^2 - 187.45\bar{s}}{\bar{s}^4 + 11.255\bar{s}^3 + 47.180\bar{s}^2 + 87.237\bar{s} + 59.977}\right)(-0.01161)$$

The contribution of $\tilde{C}_{D_{\tilde{\delta}_e^5}}(\bar{s})$ is negligible compared to the quadratic contribution.

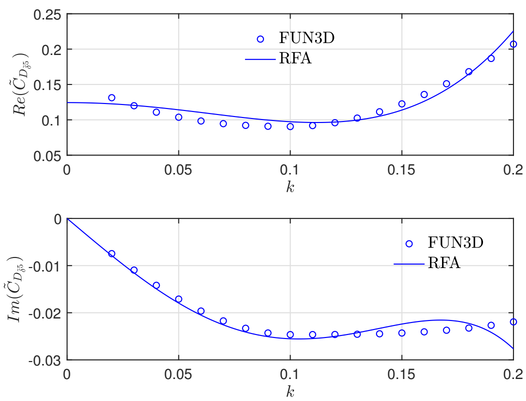

Figure 17. Frequency-Domain Regression of $\tilde{C}_{D_{\tilde{\delta}_e^5}}$

Figure 18 shows the regression of the nonlinear drag dynamic control derivative $\tilde{C}_{D_{\tilde{\delta}_e^6}}$. The estimated drag dynamic control derivative $\tilde{C}_{D_{\tilde{\delta}_e^6}}(\bar{s})$ is obtained as

$$\tilde{C}_{D_{\tilde{\delta}_e^6}}(\bar{s}) = \left(1 + \frac{135.55\bar{s}^4 + 54.869\bar{s}^3 + 9.5525\bar{s}^2 + 0.2904\bar{s}}{\bar{s}^4 + 3.1364\bar{s}^3 + 3.6887\bar{s}^2 + 1.9281\bar{s} + 0.3779}\right)(14.984 - 23.789\bar{s})$$

The individual dynamic control derivatives are obtained from $\tilde{C}_{D_{\tilde{\delta}_e^5}}(\bar{s})$ as

$$C_{D_{\delta_e^6}}(\bar{s}) = \left(1 + \frac{135.55\bar{s}^4 + 54.869\bar{s}^3 + 9.5525\bar{s}^2 + 0.2904\bar{s}}{\bar{s}^4 + 3.1364\bar{s}^3 + 3.6887\bar{s}^2 + 1.9281\bar{s} + 0.3779}\right)14.984$$

$$C_{D_{\dot{\delta}_e^6}}(\bar{s}) = \left(1 + \frac{135.55\bar{s}^4 + 54.869\bar{s}^3 + 9.5525\bar{s}^2 + 0.2904\bar{s}}{\bar{s}^4 + 3.1364\bar{s}^3 + 3.6887\bar{s}^2 + 1.9281\bar{s} + 0.3779}\right)(-23.789)$$

The contribution of $\tilde{C}_{D_{\tilde{\delta}_e^6}}(\bar{s})$ is quite large but it is still smaller than the quadratic contribution when the deflection is taken into account.

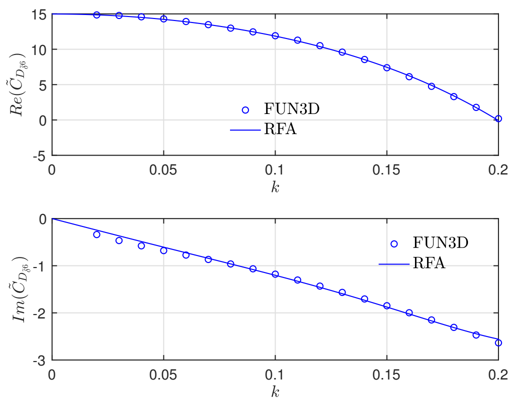

Figure 18. Frequency-Domain Regression of $\tilde{C}_{D_{\bar{\delta}_e^6}}$

4. Comparison to Steady-State Control Derivatives

Steady-state simulations of the elevator aerodynamics are conducted. Figures 19(a), (b), and (c) show the lift, drag, and pitching moment coefficients as functions of the elevator deflection, respectively. Cubic polynomials are used to curvefit the lift and pitching moment coefficients to obtain the steady-state control derivatives. A 6$^{\text{th}}$-degree polynomial is used to curvefit the drag coefficient. In general, there is agreement between the steady-state and unsteady lift and pitching moment coefficients as far as the data ranges and the shapes of the curves are concerned. For the drag coefficient, the minimum drag value of the steady-state drag coefficient is higher than that of the unsteady drag coefficient. The shape of the drag curve follows the same trend as the unsteady drag curves.

Table 1 shows the comparison between the steady-state control derivatives and the dynamic control derivatives evaluated for $\bar{s} = 0$ corresponding to the steady-state condition. There is general agreement between the two sets of control derivatives. There is also a general trend showing that the steady-state control derivatives in general are larger than the dynamic control derivatives evaluated at $\bar{s} = 0$. The differences could be due the frequency-domain regression which may not be able to capture sufficient resolution at very low frequencies near the DC value.

j	$\bar{C}_{L_{\bar{\delta}_e^j}}$	$C_{L_{\delta_e^j}}(0)$	$\bar{C}_{m_{\bar{\delta}_e^j}}$	$C_{m_{\delta_e}}(0)$	$\bar{C}_{D_{\bar{\delta}_e^j}}$	$C_{D_{\delta_e^j}}(0)$
1	0.9364	0.8648	−7.3066	−6.7936	0.005936	0.005842
2	−0.06506	−0.0298	0.8410	0.7287	0.6084	0.5867
3	−3.4207	−2.6160	26.7211	20.7786	−0.05086	−0.04918
4					−4.8338	−4.2855
5					0.1573	0.1244
6					17.9492	14.9840

Table 1. Comparison Between Steady-State and Dynamic Control Derivatives for $\bar{s} = 0$

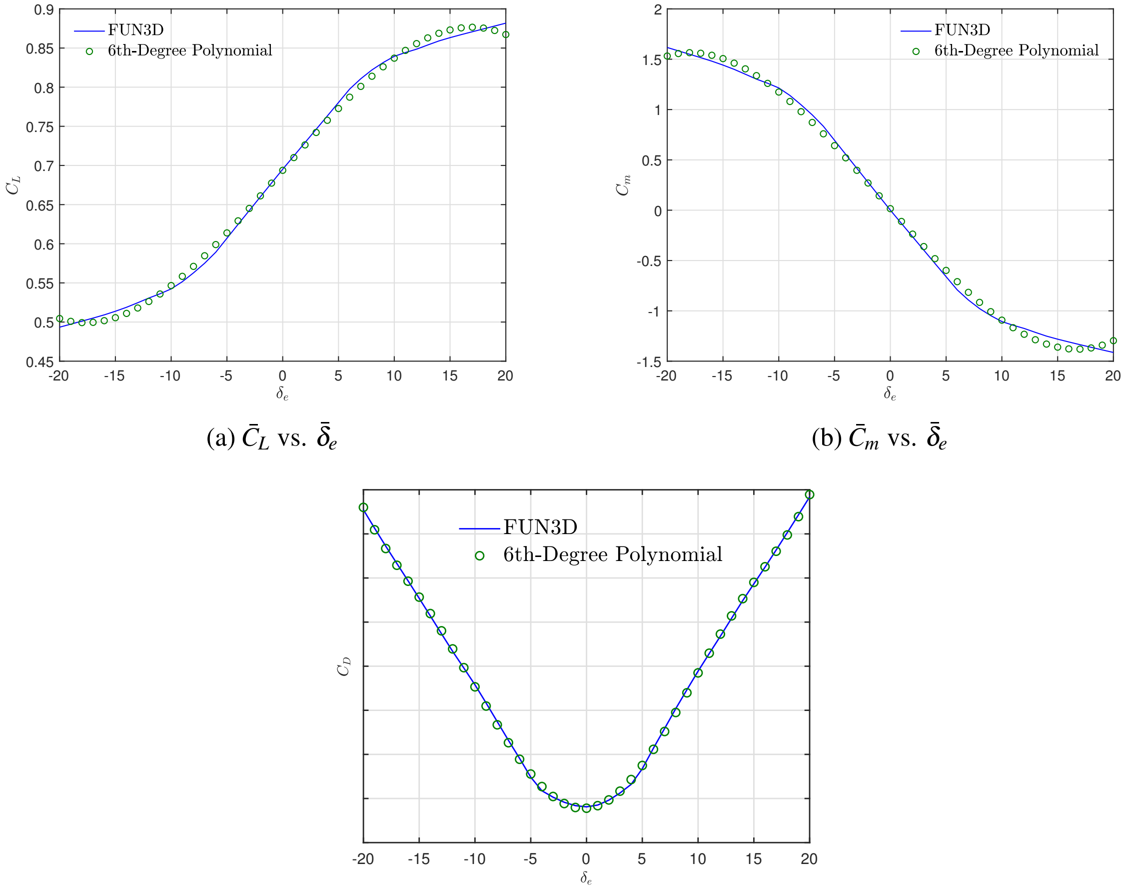

(a) $\bar{C}_L$ vs. $\bar{\delta}_e$

(b) $\bar{C}_m$ vs. $\bar{\delta}_e$

(c) $\bar{C}_D$ vs. $\bar{\delta}_e$

Figure 19. Drag Coefficient vs. Elevator Deflection for 20° Amplitude

IV. Conclusion

This paper presents a frequency-domain estimation technique for the dynamic control derivatives of aircraft. The dynamic control derivatives account for the non-circulatory lift in accordance with the Theodorsen's theory. Moreover, nonlinear dynamic control derivatives are also incorporated in the estimation to account for nonlinear effects due to flow separation associated with large control surface deflection amplitudes. Unsteady RANS CFD simulations of control surface oscillations of the elevator of the Mach 0.8 Transonic Truss-Braced Wing are conducted at various reduced frequencies. The time-domain data are transformed into the frequency-domain data by a Fourier series analysis. A frequency-domain regression is performed on the frequency-domain data. At large deflection amplitudes above 10°, the effects of flow separation at the trailing edge of the elevator become prominent particularly at the 20° deflection. The lift and pitching moment coefficients are modeled as cubic polynomials of the deflection. The drag coefficient is modeled as a sixth polynomial. In the frequency domain, these nonlinear contributions manifest themselves as higher harmonics. A complete set of linear and nonlinear dynamic control derivatives is extracted from the frequency-domain estimation.

Acknowledgment

The authors wish to acknowledge NASA Advanced Air Transport Technology project for the funding support of this work. The authors also acknowledge Boeing Research and Technology and in particular Christopher Droney, Neal Harrison, Michael Beyar, Eric Dickey, and Anthony Sclafani, along with the NASA technical POC, Gregory Gatlin, for their research conducted under the NASA BAART contracts NNL10AA05B and NNL16AA04B. The research published in this paper is made possible by the technical data and wind tunnel test data furnished under these BAART contracts.

References

[1]Wang, F., and Chen, L., "Numerical Prediction of Stability Derivatives for Complex Configurations," Procedia Engineering 99 (2015) 1561-1575.

[2]Ghoreyshi M., Bergeron K., Lofthouse, A., and Cummings R., "CFD Calculation of Stability and Control Derivatives For Ram-Air Parachutes," AIAA Applied Aerodynamics Conference, AIAA-2016-1536, 2016.

[3]Murmann, S., "A Reduced-Frequency Approach for Calculating Dynamic Derivatives," AIAA Aerospace Sciences Meeting, AIAA-2005-0840, 2005.

[4]Nguyen, N. and Xiong, J., "CFD-Based Frequency Domain Method for Dynamic Stability Derivative Estimation with Application to Transonic Truss-Braced Wing," AIAA Aviation Forum, Applied Aerodynamics, AIAA-2022-3596, June 2022.

[5]Harrison, N. A., Sclafani, A. J., Beyar, M. D., Dickey, E. D., and Intravartolo, N. M., "Subsonic Ultra Green Aircraft Research: Phase IV Final Report: Vol.2 Transonic Truss-Braced Wing High-Speed Test Report," NASA/CR-2020-000000, 2020.

[6]Theodorsen, T., "General Theory of Aerodynamic Instability and the mechanism of Flutter", NACA Report No. 496, 1949.

[7]Harrison, N. A., Gatlin, G. M., Viken, S. A., Breyar, M., Dickey, E. D., Hoffman, K., and Reichenbach, E. Y., "Development of an Efficient M=0.80 Transonic Truss-Braced Wing Aircraft," AIAA-2020-0011, January 2020.

[8]Xiong, J. and Nguyen, N., "Steady and Unsteady Simulations of Transonic Truss-Braced Wing Aircraft for Flight Dynamic Stability Analysis," AIAA Applied Aerodynamics Conference, June 2022.